



# Significant ion conduction in Cu acceptor-substituted bismuth titanate polycrystalline ceramics

Changbai Long<sup>1,2,\*</sup> , Tao Du<sup>1</sup>, and Wei Ren<sup>2,\*</sup>

<sup>1</sup>School of Advanced Materials and Nanotechnology, Xidian University, Xi'an 710071, China

<sup>2</sup>Electronic Material Research Laboratory, Key Laboratory of the Ministry of Education & International Center for Dielectric Research, Xi'an Jiaotong University, Xi'an 710049, China

**Received:** 30 November 2019

**Accepted:** 5 February 2020

**Published online:**

12 February 2020

© Springer Science+Business Media, LLC, part of Springer Nature 2020

## ABSTRACT

This paper reports that Cu acceptor substitution at the Ti site has significant effects on structure and electrical properties of Aurivillius-phase  $\text{Bi}_4\text{Ti}_3\text{O}_{12}$  polycrystalline ceramics. Phase purity, microstructure and defect chemistry of  $\text{Bi}_4\text{Ti}_{3-x}\text{Cu}_x\text{O}_{12-x}$  (BiT-100xCu,  $x = 0-0.12$ ) are characterized by XRD, SEM, EDS and EPR measurements. Neutron diffraction refinement indicates that BiT-8Cu has an orthorhombic symmetry [space group:  $B2cb$ ; lattice parameters:  $a = 5.4116(1) \text{ \AA}$ ,  $b = 32.833(1) \text{ \AA}$ ,  $c = 5.4479(1) \text{ \AA}$  and  $V = 967.98(5) \text{ \AA}^3$ ]. Impedance spectra of BiT-100xCu were measured under variable oxygen partial pressure ( $p\text{O}_2$ ).  $\text{Bi}_4\text{Ti}_3\text{O}_{12}$  shows mixed electronic (hole) and ionic conduction owing to the existence of oxygen vacancies ( $V_{\text{O}}^{\bullet}$ ) arising from the loss of  $\text{Bi}_2\text{O}_3$  during sintering. Interestingly, bulk conductivity in Cu-substituted  $\text{Bi}_4\text{Ti}_3\text{O}_{12}$  ceramics is predominately ionic due to the fact that there are considerably additional oxygen vacancies introduced into the perovskite lattices. The optimum composition of BiT-8Cu shows high ionic conductivity in the bulk with a value of  $\sim 0.007 \text{ S/cm}$  at  $650 \text{ }^\circ\text{C}$ .

## Introduction

Aurivillius-phase bismuth titanate ( $\text{Bi}_4\text{Ti}_3\text{O}_{12}$ ) is thought to be one of the most prospective lead-free ferroelectric and piezoelectric materials with potential applications in nonvolatile ferroelectric random-access memories (NvFRAMs) and high-temperature piezoelectric transducers owing to giant spontaneous polarization  $P_s$  ( $\sim 50 \mu\text{C/cm}^2$ ) and high Curie point  $T_c$  ( $\sim 673 \text{ }^\circ\text{C}$ ) of it, respectively [1–7]. It is well known that the main problem in the study of

$\text{Bi}_4\text{Ti}_3\text{O}_{12}$  ceramics and films is the fact that oxygen vacancies ( $V_{\text{O}}^{\bullet}$ ) at the lattices are readily generated owing to the evaporation of  $\text{Bi}_2\text{O}_3$  during processing. In the development of  $\text{Bi}_4\text{Ti}_3\text{O}_{12}$  materials, urgent problems that must be solved are their relatively high leakage current and high electrical conductivity that interfere with the poling process [8]. In addition, the oxygen vacancies existing at domain walls would cause a “pinning” effect against the reversal of ferroelectric domains. These disadvantages lead to relatively low remnant polarization ( $P_r \approx 7.5 \mu\text{C/cm}^2$ )

Address correspondence to E-mail: longchangbai@xidian.edu.cn; wren@xjtu.edu.cn

and low piezoelectric activity ( $d_{33} \approx 8$  pC/N) for  $\text{Bi}_4\text{Ti}_3\text{O}_{12}$  ceramics and films [6, 8–11]. It has been demonstrated that such problems can be essentially solved by lanthanoid cation isovalent substitution and/or B-site substitution, because the  $V_{\text{O}}^{\cdot\cdot}$  concentration ( $[V_{\text{O}}^{\cdot\cdot}]$ ) in the perovskite layers decreases significantly [1–4, 9–14].

Oxygen ionic conductor is one kind of important functional materials with potential applications in the field of solid oxide fuel cells (SOFCs), gas sensors, batteries, catalysts, etc. [15–18]. In the last two decades, fluorite-type  $\text{Bi}_2\text{O}_3$  and pseudo-perovskite  $\text{Bi}_4\text{V}_2\text{O}_{11}$  have attracted accumulated attention, because their high-temperature phases have high ionic conductivity [18–21].  $\text{Bi}_4\text{V}_2\text{O}_{11}$  also belongs to the family of Aurivillius compounds and consists of alternating  $(\text{Bi}_2\text{O}_2)^{2+}$  layer and the oxygen-deficient perovskite block with composition of  $(\text{VO}_{3.5}\square_{0.5})^{2-}$  ( $\square$  stands for an oxide-ion vacancy) [22]. It is demonstrated that high oxide ionic conductivity in  $\delta\text{-Bi}_2\text{O}_3$  and  $\gamma\text{-Bi}_4\text{V}_2\text{O}_{11}$  is associated with both intrinsic oxygen-deficient structures of them and high polarizability of  $\text{Bi}^{3+}$  with 6  $s^2$  lone pair electrons [19, 20, 23]. In addition, some significant researches focus on perovskite-related oxide ionic conductors, e.g.,  $\text{Na}_{0.5}\text{Bi}_{0.5}\text{TiO}_3$ -based (NBT),  $\text{LaMeO}_3$ -based (Me = Ga, Co and Fe) and  $\text{SrMeO}_3$ -based (Me = Si and Ge) materials [24–29]. It is suggested that remarkable ionic conductivity in them is primarily related to the induced extrinsic oxygen vacancies due to nonstoichiometric compositions and/or acceptor substitutions.

It is reported that  $\text{Bi}_4\text{Ti}_3\text{O}_{12}$  ceramics and signal crystals both have mixed ionic- and  $p$ -type conduction [30, 31]. High level of lanthanoid cation substitution by means of stabilizing the oxygen ions can decrease effectively  $[V_{\text{O}}^{\cdot\cdot}]$  and hole concentration ( $[h^{\cdot}]$ ) in the perovskite blocks, and consequently both leakage current and electrical conductivity ( $\sigma$ ) of  $\text{Bi}_4\text{Ti}_3\text{O}_{12}$  decrease significantly [2]. Also, the donor substitution for  $\text{Ti}^{4+}$  by higher valence cations (e.g.,  $\text{Ta}^{5+}$ ,  $\text{Nb}^{5+}$  or  $\text{W}^{6+}$ ) can effectively solve those problems [32, 33]. Here, we report that  $\text{Cu}^{2+}$  acceptor substitution for the B-site  $\text{Ti}^{4+}$  gives rise to high oxygen ion conductivity for  $\text{Bi}_4\text{Ti}_3\text{O}_{12}$ -based ceramics. The optimal composition with a nominal formula of  $\text{Bi}_4\text{Ti}_{2.92}\text{Cu}_{0.08}\text{O}_{11.92}$  shows bulk ionic conductivity of  $\sim 0.007$   $\text{S cm}^{-1}$  at 650 °C, which is close to that of  $\text{Na}_{0.5}\text{Bi}_{0.49}\text{Ti}_{0.98}\text{Mg}_{0.02}\text{O}_{2.965}$  ( $\sim 0.01$   $\text{S cm}^{-1}$ ) [27].

This work not only clarifies the importance of  $V_{\text{O}}^{\cdot\cdot}$  in the perovskite units on the electrical conductivity of  $\text{Bi}_4\text{Ti}_3\text{O}_{12}$  but also highlights the negative influence of defect dipoles on the migration of oxygen vacancies.

## Experimental procedure

Cu-substituted  $\text{Bi}_4\text{Ti}_3\text{O}_{12}$  polycrystalline ceramics were prepared by using a traditional solid-state reaction process. For preparing nominal compositions of  $\text{Bi}_4\text{Ti}_{3-x}\text{Cu}_x\text{O}_{12-x}$  ( $x = 0, 0.04, 0.08$  and  $0.12$ , abbreviated as BiT–100 $x$ Cu), the appropriate amounts of high-purity starting oxides [ $\text{Bi}_2\text{O}_3$  (99.5%),  $\text{TiO}_2$  (99.8%),  $\text{CuO}$  (99.99%)] were ball milled and then calcined in high-temperature furnace by controlling temperature at 780–820 °C for 4 h. The calcined powders were remilled in ethanol for 12 h. Then, the products were dried, ground and cold isostatically pressed into pellets at a pressure of 250 MPa. After that, the pressed pellets covered with the same calcined powders were sintered at 1000–1100 °C for 2 h. The prepared BiT–100 $x$ Cu ceramics show a relative density of  $\sim 93.5$ – $96.7\%$  (see Table 1).

For checking phase purity and calculating lattice parameters, X-ray diffraction (XRD) data (X'Pert PRO MPD, Philips, the Netherlands) of the prepared oxides were collected in  $2\theta$  range of 15°–100° with a step size of about 0.02°, the entire run lasting for 60 min. Crystal structure of selected BiT–10Cu was Rietveld refined based on powder neutron diffraction data. The data were collected from about 10 g sample on the high-resolution powder diffractometer (CAEP, Mianyang, China) at the wavelength of 1.8846 Å. Cross-sectional scanning electron microscope (SEM) images were performed by using a SEM instrument (JSM 5610, JEOL, Japan) equipped with energy-dispersive X-ray spectroscopy (EDS). Electron paramagnetic resonance (EPR) measurements were performed on a high-sensitivity X-band ( $\sim 9.2$  GHz) EPR system (JES-FA200, JEOL, Japan) at 100 K. Temperature dependences of dielectric permittivity and dielectric loss were performed on a LCR meter (4284A, Agilent, USA) at different frequencies (100, 1 k, 10 k, 100 k and 1 M Hz). The temperature ranged from room temperature to 750 °C. Impedance spectroscopy measurements under different atmospheres were performed on an impedance analyzer (20–30M Hz, Keysight, E4990A) or a Solartron 1260

**Table 1** Cation composition analysis in BiT–100xCu and relative density of them

Compositions	Bi (at.%)	Bi (at.%)	Ti (at.%)	Cu (at.%)	Relative density (%)
BiT–0Cu	Experimental	56.69 ( $\pm$ 0.38)	43.31 ( $\pm$ 0.39)	–	95.8
	Theoretical	57.14	42.86	–	
BiT–4Cu	Experimental	56.78 ( $\pm$ 41)	42.57 ( $\pm$ 32)	0.65 ( $\pm$ 43)	96.7
	Theoretical	57.14	42.29	0.57	
BiT–8Cu	Experimental	56.72 ( $\pm$ 33)	42.36 ( $\pm$ 29)	0.92 ( $\pm$ 49)	96.1
	Theoretical	57.14	41.72	1.14	
BiT–12Cu	Experimental	56.81 ( $\pm$ 43)	42.21 ( $\pm$ 42)	0.98 ( $\pm$ 52)	93.5
	Theoretical	57.14	41.15	1.71	

EDS measurements for the main phase were performed on ten randomly selected areas within grains. The mean value and standard deviation were listed. The theoretical density was determined by using refined lattice parameters, and the experimental density was measured by the Archimedes method

electrochemical workstation (0.1–5M Hz). Electrodes for electrical property measurements were fabricated with fired-on platinum (Pt) paste.

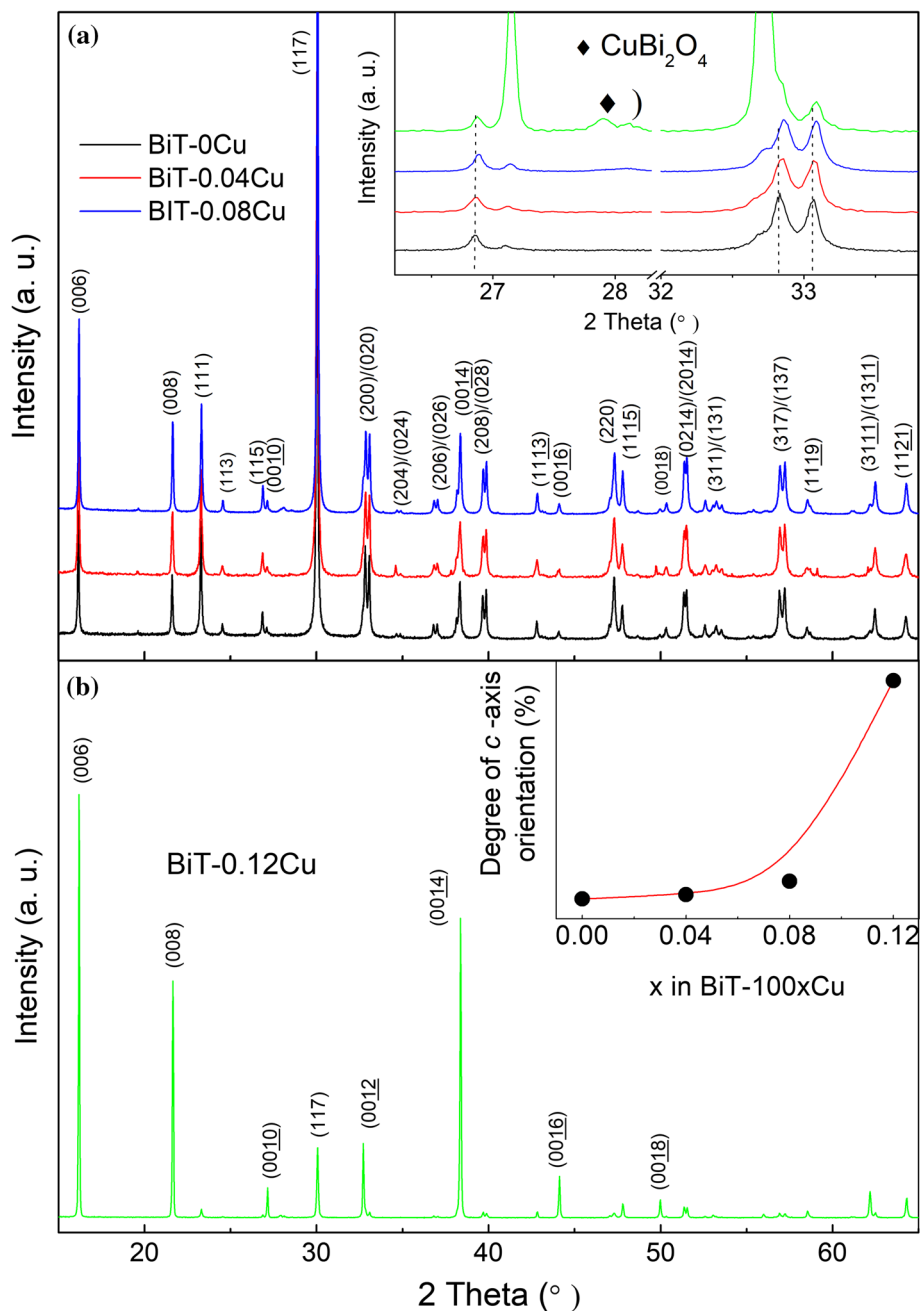
## Results and discussion

### Phase and structure

XRD patterns of BiT–0Cu, BiT–4Cu and BiT–8Cu are displayed in Fig. 1a. For each composition, it can be seen that all the diffraction peaks are in accordance with those of the orthorhombic  $\text{Bi}_4\text{Ti}_3\text{O}_{12}$  (ICSD#01-072-1019), implying that there is no evidence of any impurity phase induced by lower level of Cu substitution. However, higher level of Cu substitution leads to generation of impurity-phase  $\text{CuBi}_2\text{O}_4$  at the  $2\theta$  angle of  $\sim 28^\circ$  in the XRD pattern of BiT–12Cu (inset of Fig. 1a). In addition, BiT–12Cu ceramic shows significant  $c$ -oriented grain growth (see Fig. 1b). The intensity of (00  $l$ ) diffraction peaks of it such as (006), (008) and (0014) is much higher than that of the major (117) peak. However, the case is adversely observed for the other compositions. Figure 2a–c demonstrates cross-sectional SEM images of the polished BiT–4Cu, BiT–8Cu and BiT–12Cu ceramics, respectively. The results reveal that there are some amounts of impurity phases (dark) presented in BiT–8Cu and BiT–12Cu rather than in BiT–4Cu. EDS analysis by line scanning indicates that CuO is the main impurity phase (Fig. 2d). It is suggested that the maximum  $x$  for Cu substitution at the Ti site within solid solution limit is between 0.04 and 0.08.

Grain size of BiT–100xCu ceramics firstly decreases and then increases as  $x$  value increases in BiT–100xCu (Fig. 3). For BiT–12Cu, the ratio of length to thickness of grains ( $L/t$ ) is  $\sim 30$ –50, and the great majority of grains are overlarge and laminated (Fig. 3d). It is presumable that excess CuO acts as effective flux agents functioning as lowering temperature for ceramics' sintering [34]. As a consequence, the laminated grains stacking together lead to the fact that BiT–12Cu ceramics are highly textured. Based on the XRD data (see Fig. 1), the degree of orientation of BiT–100xCu ceramics can be calculated by using the Lotgering orientation factor ( $f$ ) [35]. Value of BiT–100xCu in the  $c$ -axis direction is  $\sim 74.4\%$ , much higher than that of the other compositions ( $\sim 15.6$ –20.5%) (inset of Fig. 1b). Moreover, the main phase composition of all ceramic samples was characterized by point EDS analysis. After the cation ratios being normalized to 100%, the results of BiT–100xCu are listed in Table 1. For BiT–4Cu and BiT–8Cu, the experimental percentage of Cu is close to the theoretical one. This value of BiT–12Cu is  $\sim 0.98$  at.%, much lower than the theoretical percentage ( $\sim 1.71$  at.%). In addition, the Bi percentage of all compositions is  $\sim 56.69$ –56.81 at.%, which is lower than the theoretical value of them (57.14 at.%) due to the loss of  $\text{Bi}_2\text{O}_3$  during processing. Lattice parameters ( $a$ ,  $b$ ,  $c$ ) of BiT–100xCu are calculated based on the XRD data, as shown in Fig. 4a. It is clear that an increase in  $x$  value in BiT–100xCu results in increase in  $a$  and  $b$  but gradual decrease in  $c$ . In general, the unit cell volume ( $V$ ) increases as  $x$  value increases. This is primarily due to the fact that the ionic radius

**Figure 1** XRD ( $\text{Cu K}\alpha_1$ ) patterns of BiT–100xCu. **a** BiT–0Cu, BiT–4Cu and BiT–8Cu; **b** BiT–12Cu. In **a**, an inset shows an impurity phase of  $\text{CuBi}_2\text{O}_4$  at  $2\theta = \sim 28^\circ$  for BiT–12Cu. In **b**, an inset shows degree of  $c$ -axis orientation for BiT–100xCu.

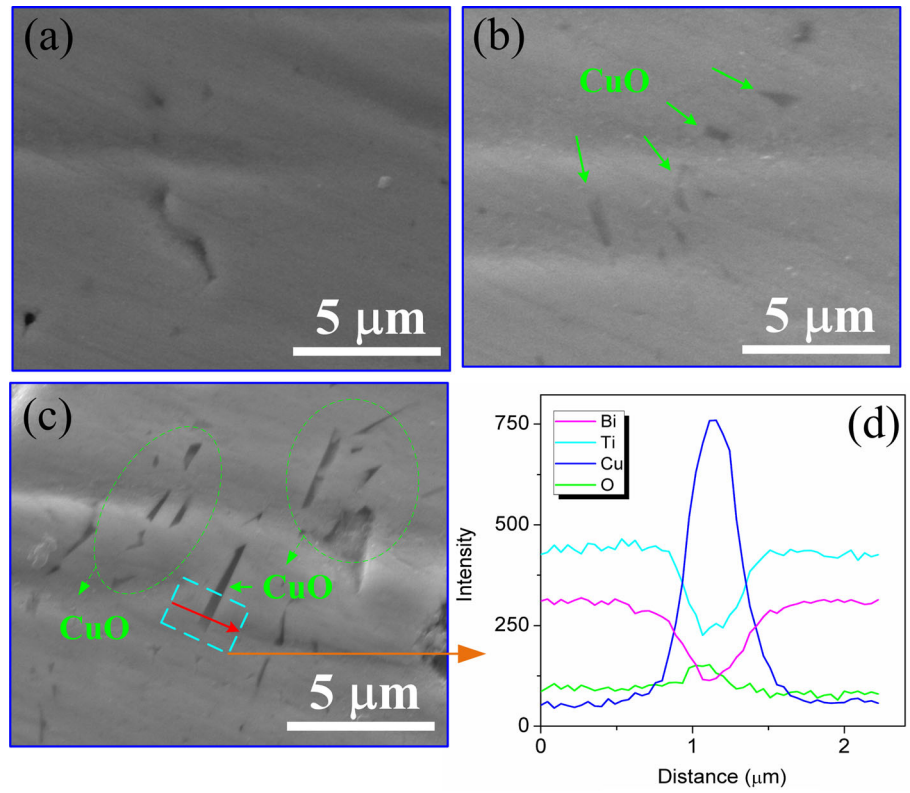


of  $\text{Cu}^{2+}$  is larger than that of  $\text{Ti}^{4+}$  at the B site ( $\text{Cu}^{2+}$ : 0.73 Å,  $\text{Ti}^{4+}$ : 0.605 Å; 6 CN) [36].

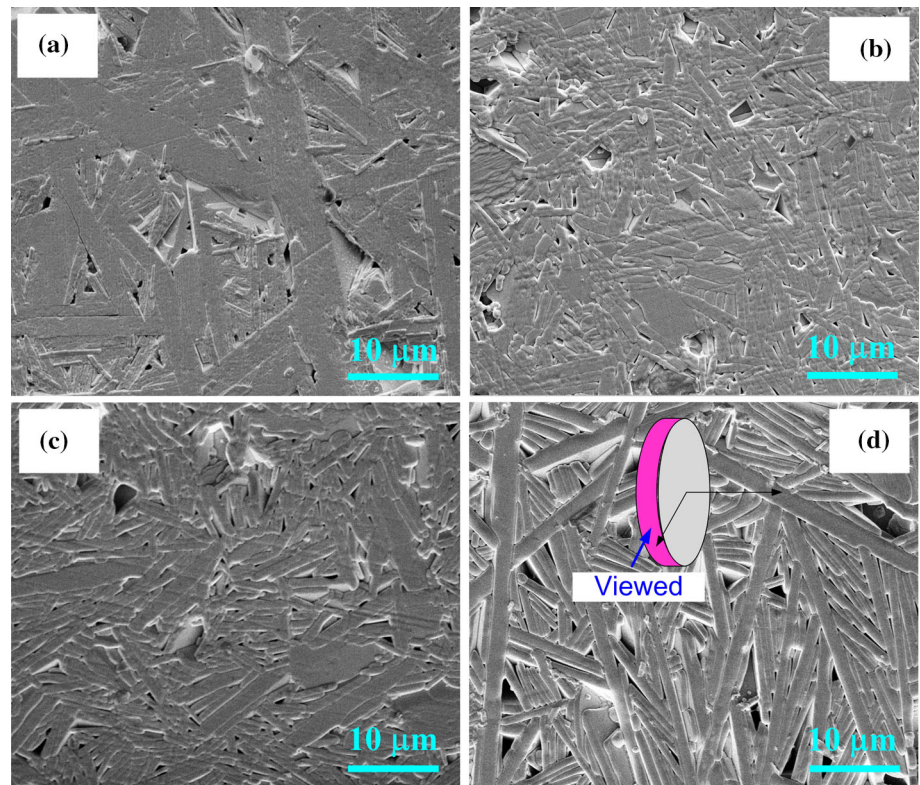
Based on neutron powder diffraction data, Rietveld refinement for BiT–8Cu was carried out by using the GSAS program. The orthorhombic structure of  $\text{Bi}_4\text{-Ti}_3\text{O}_{12}$  (space group  $Aba2$ ; ICSD #87808) reported by Hervoches et al. was adapted as an initial model, where small parts of Ti atoms were replaced by Cu atoms at the B site. The refined profile together with the experiment one is displayed in Fig. 4b. For this refinement, the agreement factors were  $R_{\text{wp}} = 3.94\%$ ,

$R_p = 3.06\%$  and  $D_{\text{wd}} = 1.739$ . Refining the Bi occupancy reveals that value for the Bi1 site in the perovskite layer is lower than that for the Bi2 site in the  $(\text{Bi}_2\text{O}_2)^{2+}$  layer. This may be attributed to lower formation energies of bismuth vacancy ( $V_{\text{Bi}}^{\prime\prime}$ ) and oxygen vacancy ( $V_{\text{O}}^{\bullet}$ ) in the  $(\text{Bi}_2\text{O}_2)^{2+}$  layer [37]. The refined occupancy at the O1–O6 sites is about 0.986, and the Cu occupancy at the Ti1 and Ti2 sites is about 0.007 and 0.032, respectively. As a consequence, BiT–8Cu changes into  $\text{Bi}_{3.932}\text{Ti}_{2.929}\text{Cu}_{0.071}\text{O}_{11.832}$ , which is close to the measured composition for the main phase

**Figure 2** Cross-sectional SEM images (secondary electron) of Cu-substituted compositions, **a** BiT–4Cu, **b** BiT–8Cu and **c** BiT–12Cu (polished without thermal etching). **d** EDS line scan of the dotted frame in **c**. In **b** and **c**, impurity phase of CuO (dark) is marked as green arrows in BiT–8Cu and BiT–12Cu.



**Figure 3** Cross-sectional SEM images of BiT–100xCu ceramics after polishing and thermal etching, **a**  $x = 0$ , **b**  $x = 0.04$ , **c**  $x = 0.08$  and **d**  $x = 0.12$ .



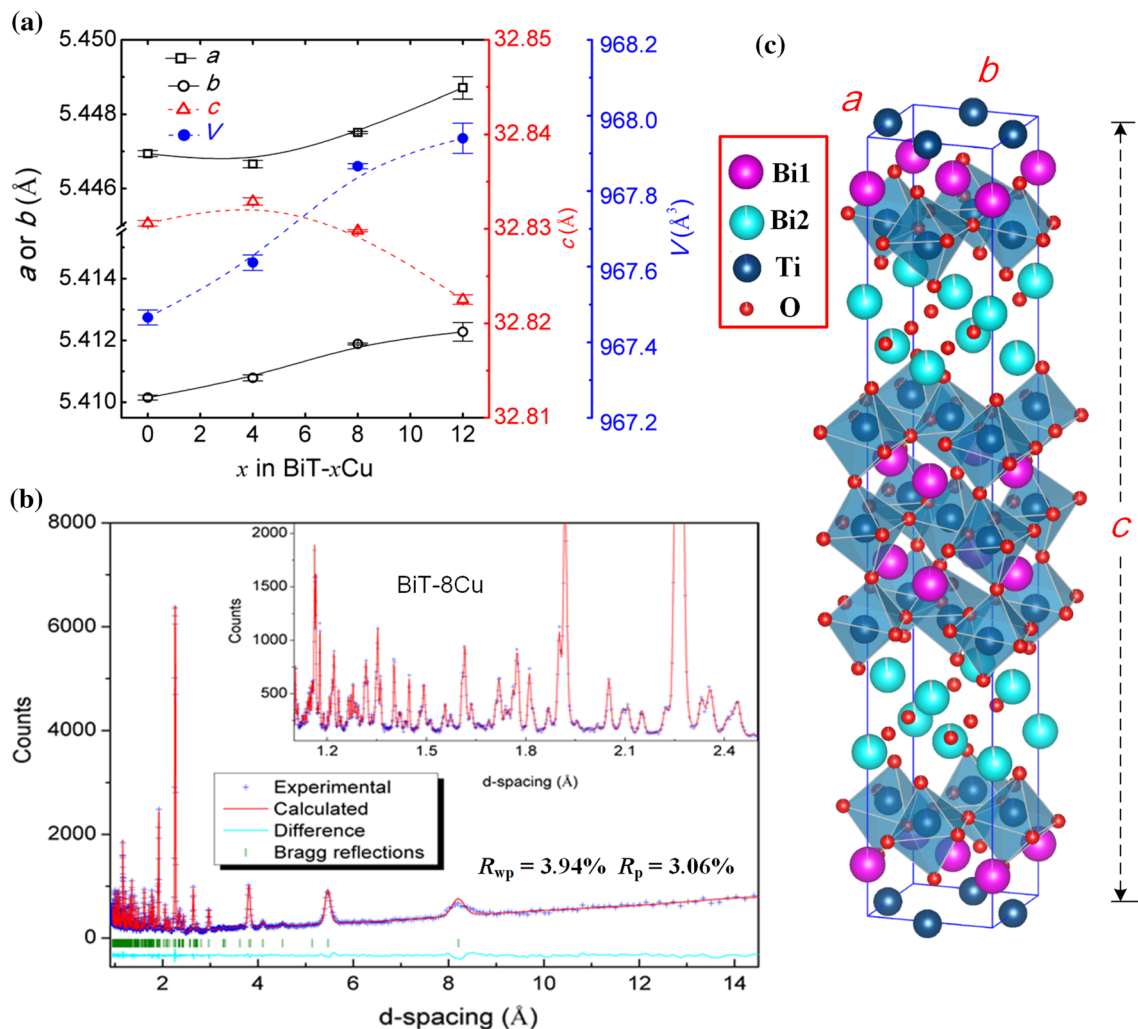


**Figure 4** **a**  $a$ ,  $b$  and  $c$  as well as  $V$  of BiT-100 $x$ Cu. **b** Neutron diffraction refinement for BiT-8Cu with an inset showing regionally enlarged drawing. **c** Crystal structure of BiT-8Cu at room temperature.

by EDS analysis ( $\text{Bi}_{3.932}\text{Ti}_{2.936}\text{Cu}_{0.064}\text{O}_{11.834}$ ). Crystal structure of BiT-8Cu is illustrated in Fig. 4c based on the refined structural parameters (see Table 2). One can see that the  $(\text{Ti,Cu})\text{O}_6$  octahedra are pronouncedly distorted and tilted away from the  $c$ -axis. This orthorhombic deformation is primarily attributed to the fact that in the ferroelectric of BiT-8Cu, the lone pair of the  $\text{Bi}^{3+}$   $6s^2$  electrons at the A site is oriented along the polarization axis [38].

### Dielectric permittivity and Dielectric loss

In Fig. 5a, temperature dependence of dielectric permittivity ( $\epsilon'$ ) at 100 kHz reveals a high-and-sharp dielectric permittivity peak between 600 and 700 °C for BiT-100 $x$ Cu, corresponding to the ferroelectric-to-paraelectric phase transition. Pure BiT-0Cu shows a

$T_c$  of  $\sim 670$  °C, being consistent with that reported by Yan et al. [6]. With the introduction of Cu substitution,  $T_c$  of BiT-4Cu and BiT-8Cu decreased to  $\sim 654$  and  $\sim 661$  °C, respectively. Shimakawa et al. [39] and Sivakumar et al. [40] suggested that the replacement of B-site cation by another one(s) with larger size leads to the enhanced structural distortion as well as the increased phase temperature for Aurivillius-phase ferroelectrics. Distinctly, this is not the case. The decreased  $T_c$  for BiT-4Cu and BiT-8Cu is probably associated with an enhancement in structure disordering because the increase in  $[\text{V}_\text{O}]$  resulted from Cu acceptor substitution [8]. Moreover, these Cu-substituted compositions show significant  $\epsilon'_{\text{max}}$  (maximum  $\epsilon'$  around  $T_c$ ) of  $\sim 1837$ -3040, much higher than that of BiT-0Cu ( $\sim 760$ ) (inset of Fig. 5a). However,  $T_c$  of BiT-12Cu increases abnormally,

**Table 2** Neutron refinement atom parameters for BiT–8Cu at room temperature

Atom	Site	<i>x</i>	<i>y</i>	<i>z</i>	<i>U</i> <sub>iso</sub>	Occupancy
Bi1	8	1.001 (1)	0.0662 (1)	0	0.0061 (6)	0.991 (3)
Bi2	8	0.019 (1)	0.2113 (1)	0.008 (1)	0.0072 (6)	0.975 (3)
Ti1	4	0	0.5	0.055 (2)	0.001 (2)	0.993 (4)
Cu1	4	0	0.5	0.055 (2)	0.001 (2)	0.007 (4)
Ti2	8	– 0.005 (2)	0.3704 (3)	0.053 (2)	0.002 (2)	0.968 (4)
Cu2	8	– 0.005 (2)	0.3704 (3)	0.053 (2)	0.002 (2)	0.032 (4)
O1	8	0.265 (1)	0.0062 (2)	0.319 (1)	0.020 (2)	0.986 (2)
O2	8	0.262 (1)	0.2489 (3)	0.260 (1)	0.003 (2)	0.986 (2)
O3	8	0.068 (1)	0.4395 (2)	0.092 (1)	0.011 (1)	0.986 (2)
O4	8	0.947 (1)	0.3195 (2)	0.055 (2)	0.003 (1)	0.986 (2)
O5	8	0.262 (2)	0.1108 (2)	0.279 (1)	0.018 (1)	0.986 (2)
O6	8	0.200 (1)	0.8749 (2)	0.211 (1)	0.013 (2)	0.986 (2)

Here, the Bi<sub>4</sub>Ti<sub>3</sub>O<sub>12</sub> coordinates in space group *Aba2* (ICSD #87808) were used as an initial model (this structure was transformed from space group *B2cb* to *Aba2* by rotating axes and coordinates according to *abc = b'c'a'*). And the occupancy of oxygen at the O1–O6 sites is uniformly released under the constraint of charge neutrality, i.e., [V<sub>O</sub><sup>•</sup>] = 1.5[V<sub>Bi</sub><sup>'''</sup>] + [Cu<sub>Ti</sub><sup>''</sup>]

Lattice parameters: *a* = 5.4116(1) Å, *b* = 32.833(1) Å, *c* = 5.4479(1) Å, *V* = 967.98(5) Å<sup>3</sup>, *Z* = 4. Reliability factors: *R*<sub>wp</sub> = 3.94%, *R*<sub>p</sub> = 3.06% and *D*<sub>w</sub> = 1.739. Space group: *Aba2*

whereas ε'<sub>max</sub> of it decreases dramatically with higher *x* value in BiT–100*x*Cu. Values of it are ~ 667 °C and ~ 831, respectively, being close to those of BiT–0Cu.

Temperature dependence of dielectric loss (tanδ) for BiT–100*x*Cu is shown in Fig. 5b. BiT–4Cu and BiT–8Cu both have much high dielectric loss. The loss tangent (tan δ) of BiT–8Cu is higher than 2.8 above ~ 550 °C and nearly goes up exponentially with temperature above *T<sub>c</sub>*, where conduction loss is very significant. In contrast, the dielectric loss of the *c*-oriented BiT–12Cu is lower, which should be attributed to the fact that the electrical properties of the layer-structured materials are dominated in the *a*–*b* plane (normal to *c*-axis) [7, 30]. For each composition, there is a relaxation peak locating at 300–500 °C in the *T* versus tanδ plot and more distinct relaxation peak is clearly observed with decreasing frequency. The results of BiT–8Cu as shown in the inset of Fig. 5b reveal that this peak goes toward lower temperature with decreasing frequency, implying that it depends on the measured frequency. This characteristic should be related to the relaxation of oxygen vacancies in materials (mainly in the bulk), which is the same as the results of Shulman et al. and Fouskova et al. [8, 41]. The activation energy for the dielectric relaxation can be estimated with the Arrhenius relationship of the relaxation time (τ = 1/

2π*f*) versus the peak temperature (the relaxation peak has the highest loss at this point):

$$\tau = \tau_0 \exp\left(\frac{E_a}{KT}\right) \tag{1}$$

Here, *K* and τ<sub>0</sub> are the Boltzmann constant and time constant, respectively. This activation energy is ~ 0.73 eV for the relaxation of V<sub>O</sub><sup>•</sup> at the low-temperature segment (~ 100–500 °C) (inset of Fig. 5b), which is consistent with the results of LaGaO<sub>3</sub> [42].

### Impedance spectra and bulk conductivity

Complex impedance spectra (*Z*<sup>\*</sup>) of BiT–100*x*Cu at 500 °C are displayed in Fig. 6a–d. In Fig. 6a, BiT–0Cu without Cu substitution shows three poorly resolved arcs as well as a weak Warburg-like element at the lowest frequencies. The leftmost arc at the high frequency range should result from the grain (bulk) response, whereas the one at the middle frequency range should result from the grain-boundary response. The rightmost arc at the left hand of the small Warburg-like spike shows capacitance with a value of ~ 5 × 10<sup>–6</sup> F/cm, which is possibly ascribed to the fact that an exchange of oxygen between the O<sub>2</sub> in the atmosphere and the O<sup>2–</sup> anions in the ceramic samples occurs. The size of this arc should be equivalent to the charge transfer resistance (*R*<sub>ct</sub>) [43].

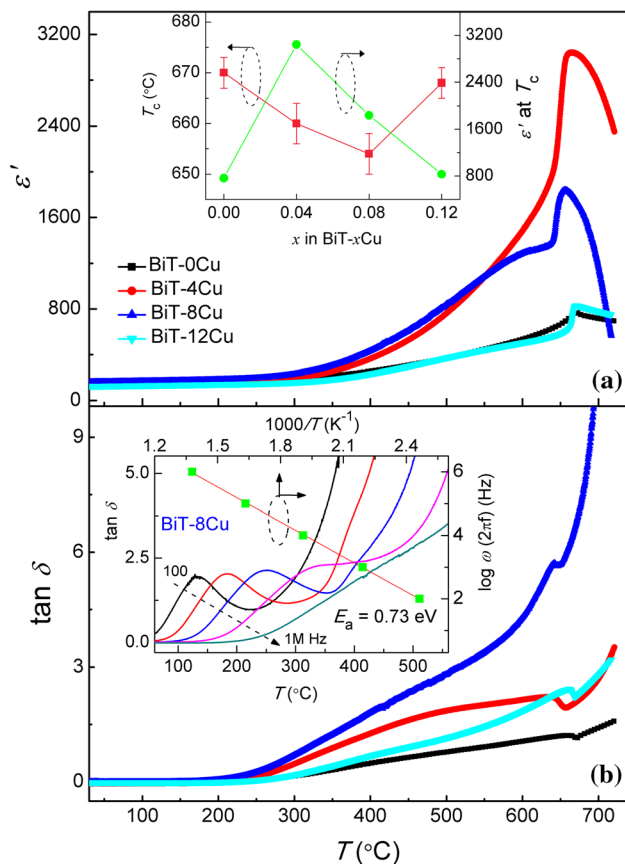


**Figure 5** Dielectric properties of BiT-100xCu at 100 kHz. **a** dielectric permittivity ( $\epsilon'$ ) and extracted  $T_c$  and maximum  $\epsilon'$  (at  $T_c$ ) as an inset. **b** Dielectric loss ( $\tan\delta$ ) with an inset showing frequency-dependent loss peak for BiT-8Cu in the low-temperature segment.

However, this response becomes rather weak and associated  $R_{ct}$  is rather low with Cu substitution (Fig. 6b, c). In the complex  $Z^*$  plots of BiT-4Cu and BiT-8Cu, three main arcs correspond to three different component effects, i.e., grain (bulk), grain boundary and electrode-sample interface effects which locate at the high, middle and low frequency ranges, respectively. Simultaneously, there are three relevant capacitance plateaus in the 500 °C capacitance ( $C'$ ) plots of them (Fig. 6f). Inspection from the figures reveals that Cu substitution leads to the decrease in the size of the bulk response arc and consequently the arc associated with the grain boundary response is relatively enlarged. Bulk resistivity ( $R_b$ ) of BiT-4Cu and BiT-8Cu is calculated roughly to be  $\sim 0.8$ – $1.2$  k $\Omega$  cm, which is about a tenth part of that of BiT-0Cu ( $\sim 9.8$  k $\Omega$  cm). In contrast, BiT-12Cu shows a large arc with  $R_b$  of  $\sim 4.5$  k $\Omega$  cm at high frequencies due to high  $c$ -axis orientation,

and the  $R_{GB}$  (grain boundary resistance) and  $R_{ct}$  arcs are poorly resolved at middle frequencies (Fig. 6d). In Fig. 6a and d, the  $R_b$  arc is distorted because the two conducting parts (ionic and electronic) together contribute to the total grain conductivity of BiT-0Cu and BiT-12Cu [31]. The impedance spectra of BiT-100xCu at 500 °C were fitted with modified Randles equivalent circuit I or II (Fig. 7). Circuit I was used to fit the experimental data for BiT-0Cu and BiT-12Cu but circuit II for the other two compositions. For each composition, the calculated and experimental data are nearly identical (see Fig. 6a–d). At higher temperature up to 725 °C, the grain boundary response disappears in the impedance spectra of BiT-0Cu and BiT-8Cu (Fig. 6e). In this case, BiT-8Cu shows two incomplete arcs associated with the bulk and electrode responses due to the limit of the measurement frequency. The  $R_{ct}$  arc still appears on the plot of BiT-0Cu, and the bulk response is the main component (inset of Fig. 6e).

More generally, the electrical properties including leakage current and conductivity of materials are very susceptible to the defects (mainly oxygen vacancies), which in turn are functions of the oxygen partial pressure ( $pO_2$ ). Figure 8a and 8b displays the impedance spectra of selected BiT-0Cu and BiT-8Cu measured at 650 °C under different atmospheres (air,  $N_2$  and  $O_2$ ), respectively. The low-frequency data of them associated with the electrode-sample interface effect both show a strong dependence on  $pO_2$ . For BiT-8Cu, the small arc under air and  $O_2$  changes into an inclined spike under  $N_2$  owing to the limited ion incorporation into a partially blocking electrode [44]. In addition, the bulk resistivity of BiT-8Cu nearly remains unchanged as the atmosphere varies from air/ $O_2$  to  $N_2$ . Similar impedance data have been reported for typical ionic conducting oxides [25, 27]. It is suggested that the bulk of BiT-8Cu is characteristic of predominately ionic conduction. It is widely accepted that a decrease in  $pO_2$  gives rise to the fact that the hole conductivity ( $\sigma_{hole}$ ) decreases but the ionic conductivity ( $\sigma_{ion}$ ) remains unchanged [45, 46]. Here, the total conductivity ( $\sigma_{total}$ ) of BiT-0Cu can be estimated with a relationship of  $\sigma_{total} = \sigma_{ion} + \sigma_{hole} [pO_2 \text{ (atm)}]^{1/6}$  [45]. In Fig. 8c, it is observed that BiT-0Cu demonstrates ionic-and-hole mixed conduction, because its bulk conductivity ( $\sigma_b$ ) decreases partially with decreasing  $pO_2$ . In contrast,  $\sigma_b$  of BiT-8Cu remains constant of  $\sim 0.007$  S  $cm^{-1}$ , implying that the ionic conduction dominates the



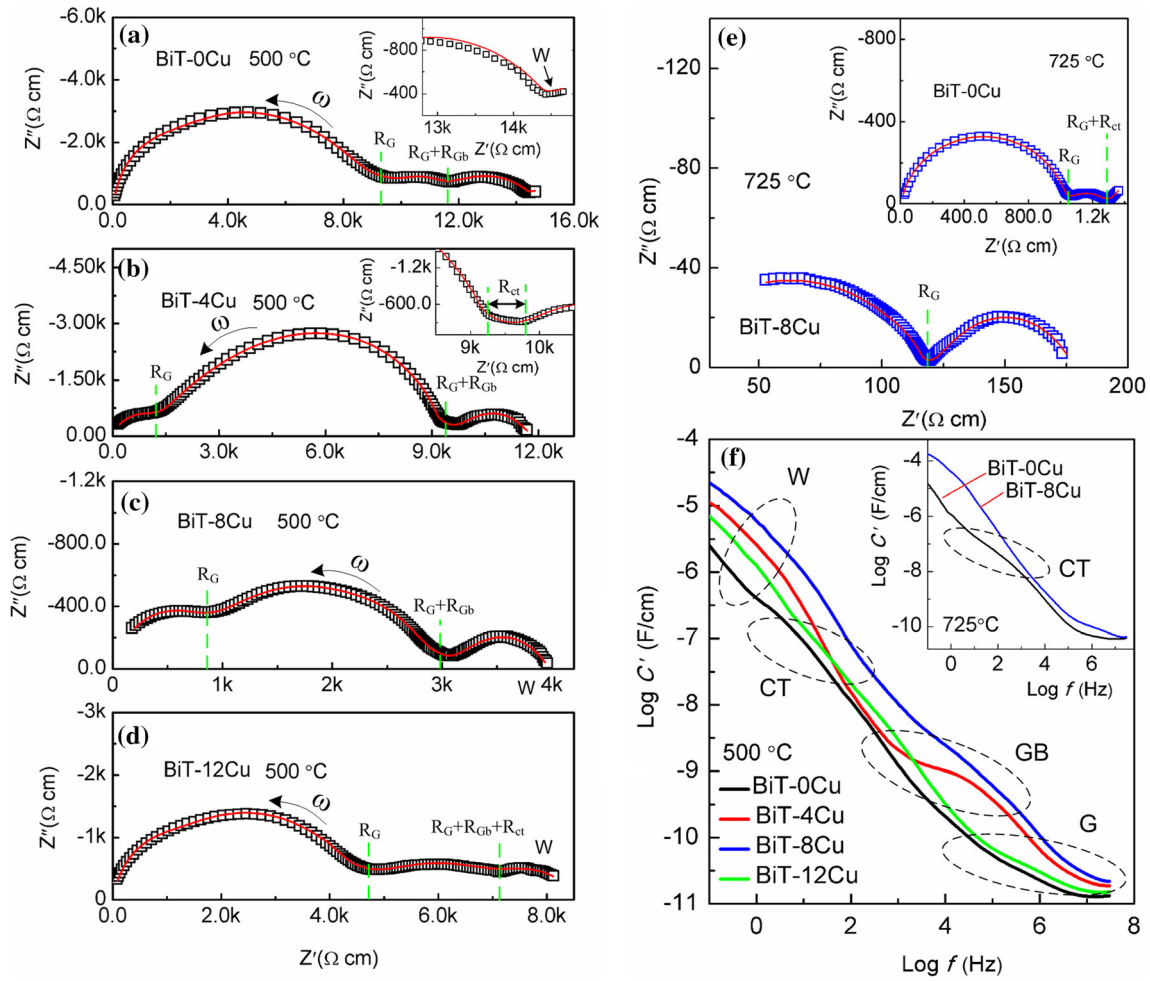


**Figure 6** a–d Complex  $Z^*$  plots of BiT–100xCu at 500 °C, and insets in a and b show regionally enlarged drawings. e Complex  $Z^*$  plots of BiT–0Cu (inset) and BiT–8Cu at 725 °C. f 500 °C  $C'$

spectroscopic plots of BiT–100xCu, and an inset shows 725 °C  $C'$  spectroscopic plots of BiT–0Cu and BiT–8Cu. In a–e, symbols are the experimental data, whereas red lines are the calculated data.

bulk. But its grain boundary conductivity ( $\sigma_{GB}$ ) decreases dramatically, because the hole conductivity is significant at the grain boundary range. It is speculated that this significant conductivity makes the strongly inclined spike under  $N_2$  turn over the arc under air/ $O_2$  (at lowest frequencies). Therefore, the total conduction of the sample appears to be ionic under  $N_2$ , whereas it changes into a mixed electronic-and-ionic conductor under air/ $O_2$ .

Commonly, the electrodes are obeying an ion-blocking condition but “reversible” for electrons. In this scenario, ionic transference number ( $t_{ion}$ ) can be derived from the Warburg-like impedance in the  $Z'$  versus  $Z''$  plots, which is described in detail elsewhere [47, 48]. As sketched in Fig. 8e, for nonblocked carrier species (electronic), the sum resistivity ( $R^{eon} = R_G^{eon} + R_{GB}^{eon}$ ) in materials is equivalent to the

zero-frequency intersection of impedance data on the  $Z'$ -axis. For total carrier species including ions and electrons (holes), the sum resistivity in materials ( $R^{tot} = R_G^{tot} + R_{GB}^{tot}$ ) corresponds to the low-frequency part intersection of grain-boundary semicircle on the  $Z'$ -axis. In addition, impedance data can be transformed into the admittance data, and the 650 °C  $Y'$  versus  $Y''$  plots of BiT–8Cu under different atmospheres were drawn. Figure 8d intuitively shows the ionic and electronic components of the total conductivity. Here, the interval of the Warburg element projected on the real axis corresponds to the conductivity of ionic species ( $\sigma_{ion}$ ) but the zero-frequency intersection of admittance data on the  $Y'$ -axis is equal to the conductivity of electronic species ( $\sigma_{econ}$ ) [49]. As a consequence,  $t_{ion}$  can be calculated with the following equation:

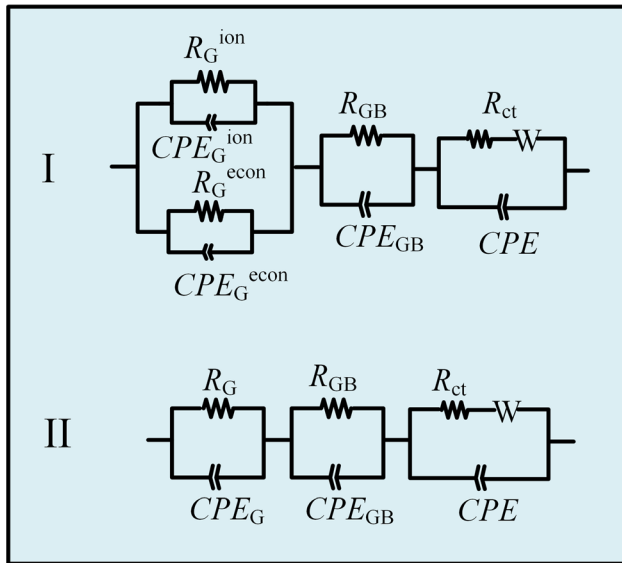


**Figure 7** Modified Randles equivalent circuits were used to calculate the impedance data of BiT–100xCu at 500 °C.

$$t_{ion} = \frac{\sigma_{ion}}{\sigma_{tot}} = \frac{\sigma_{ion}}{\sigma_{ion} + \sigma_{econ}} \quad (2)$$

where  $\sigma_{tot}$  is the total conductivity contributing from both ionic and electronic species. Inspecting the figure, a relationship of  $\sigma_{tot} \approx \sigma_{ion}$  indicates that  $t_{ion}$  is nearly the unit with negligible electronic conductivity under N<sub>2</sub>. However,  $t_{ion}$  decreases dramatically under the oxide atmospheres due to the increased hole conductivity. This value is estimated to be ~ 0.34 and ~ 0.29 under air and O<sub>2</sub>, respectively.

Arrhenius  $\sigma_b$  plots of BiT–100xCu at 250–800 °C are shown in Fig. 8f. It can be seen that  $\sigma_b$  of BiT–4Cu and BiT–8Cu increases by Cu<sup>2+</sup> substitution for the B-site Ti<sup>4+</sup>, being about ten times that of BiT–0Cu. This improvement is primarily associated with the increased [V<sub>O</sub>•] at the lattices. However,  $\sigma_b$  of BiT–12Cu with higher level of Cu substitution decreases

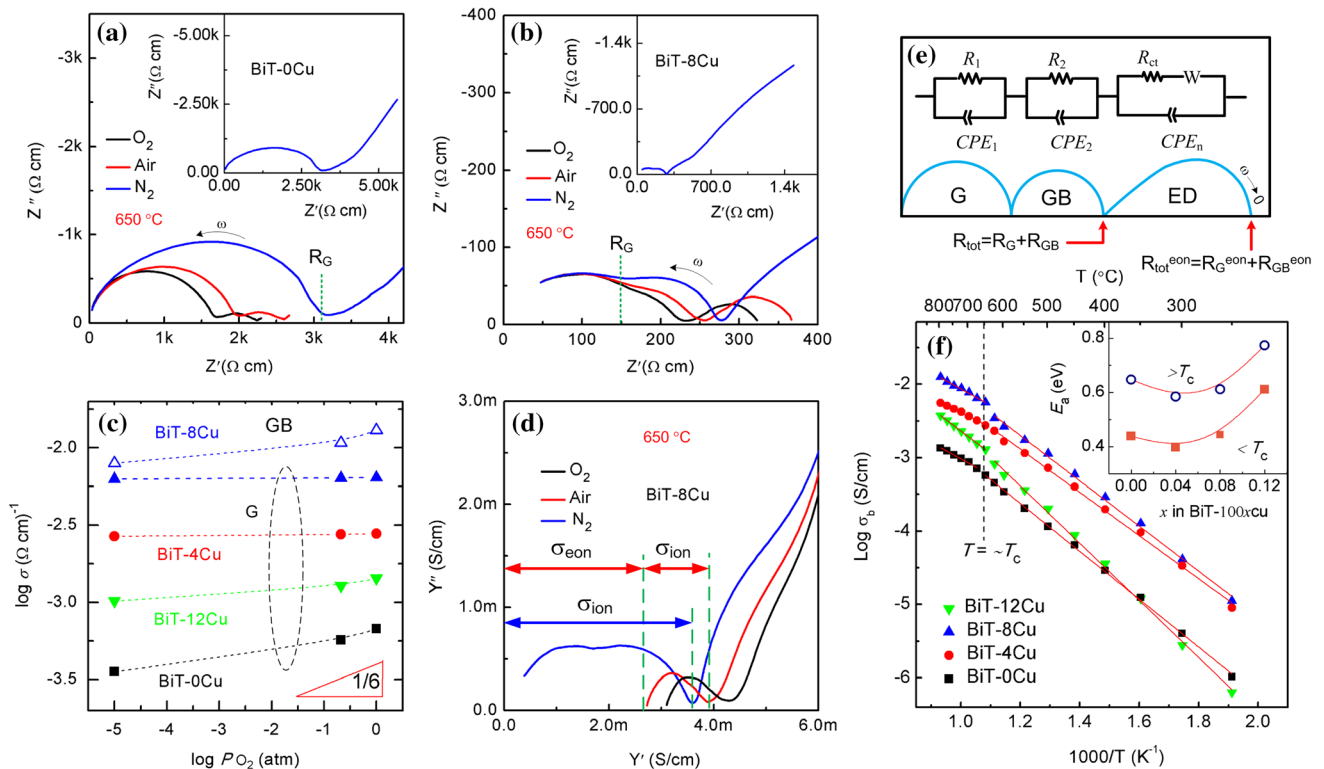
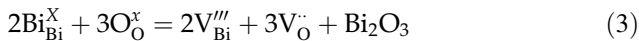


**Figure 8** a–b Z\* plots of BiT–0Cu and BiT–8Cu, c  $\sigma_b$  and  $\sigma_{GB}$  of BiT–100xCu and d Y' versus Y'' plots of BiT–8Cu at 650 °C, under N<sub>2</sub>, air and O<sub>2</sub>. e Schematic impedance spectrum for mixed conduction in the polycrystalline ceramic with ion-blocking electrode. f Arrhenius  $\sigma_b$  plots for BiT–100xCu with an inset

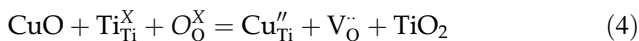
showing variable  $E_a$  as x increases in BiT–100xCu. Here, the grain, grain boundary and electrode components contributing to the total resistivity or conductivity are abbreviated as “G,” “GB” and “ED,” respectively.

abnormally. This is consistent with the change trend in the dielectric loss (Fig. 5b). Takahashi et al. [45] revealed that the conductivity of BiT–0Cu single crystals along the perovskite slabs (i.e., along the *a*–*b* plane) is ~ 2–3 orders of magnitude higher than that in the *c*-axis direction. Therefore, the decreased  $\sigma_b$  in BiT–12Cu seems to be associated with the *c*-oriented grain growth of it. For each composition, the plot of  $\log \sigma_b$  versus  $1000/T$  shows different linear relationships below and above  $T_c$ . Consequently, the activity energy ( $E_a$ ) in the low-temperature ( $< T_c$ ) and high-temperature ( $> T_c$ ) segments is different.  $E_a$  of BiT–0Cu, BiT–4Cu and BiT–8Cu is ~ 0.58–0.64 eV and ~ 0.4–0.44 eV below and above  $T_c$ , respectively. In contrast,  $E_a$  of BiT–12Cu increases to ~ 0.77 eV and ~ 0.61 eV, respectively. These higher values for the *c*-oriented BiT–12Cu are primarily attributed to the fact that the  $(\text{Bi}_2\text{O}_2)^{2+}$  layer acts as a barrier against the charge transport. Also, that trapping of charged carriers by  $\text{Cu}_{\text{Ti}}''$  leads to higher  $E_a$ .

Commonly, high  $[\text{V}_\text{O}^\bullet]$  can facilitate the movement of  $\text{O}^{2-}$  or the migration of  $\text{V}_\text{O}^\bullet$  in the oxide materials. In BiT–0Cu, the production of  $\text{V}_\text{O}^\bullet$  is primarily associated with the loss of  $\text{Bi}_2\text{O}_3$  during sintering, which is associated with the following reaction:



The resulting oxygen vacancies possibly exist at the lattices of both perovskite and  $(\text{Bi}_2\text{O}_2)^{2+}$  layers. It is likely that the migration of  $\text{O}^{2-}$  would adopt an appropriate pathway with the lowest barrier energy. For Aurivillius-phase materials with layered perovskite structure, this pathway involves a zigzag-type mechanism of the  $\text{O}^{2-}$  ion hopping from the apical site to the adjacent equatorial one in the octahedron [50]. Probably, the  $[\text{V}_\text{O}^\bullet]$  at the perovskite lattices of BiT–0Cu is relatively low. The replacement of each  $\text{Ti}^{4+}$  ion by  $\text{Cu}^{2+}$  at the B site can lead to an additional  $\text{V}_\text{O}^\bullet$ :



It is likely that the resulting  $\text{V}_\text{O}^\bullet$  inhabits the corresponding lattice in the perovskite layer [51]. Li et al. [27] suggested that high polarizable  $\text{Bi}^{3+}$  cations and weak Bi–O bonds both promote the migrating  $\text{O}^{2-}$  ions passing through an opening of a triangle defined between two A cations and one B cation (i.e., the saddle point). Moreover, the exchange of  $\text{V}_\text{O}^\bullet$  between the perovskite layer and  $(\text{Bi}_2\text{O}_2)^{2+}$  layer probably

occurs at high temperature [52]. Above  $T_c$ , the combination of these beneficial effects seems to lead to significant ionic conductivity for BiT–0.08Cu.

However, the lone electron pair ( $6s^2$ ) of  $\text{Bi}^{3+}$  at the A site will be reoriented along the polarization axis below  $T_c$ . Meanwhile, a ferroelectricity is generated in BiT–100xCu due to an orthorhombic deformation. It is observed from Fig. 9a (left) that the  $(\text{Ti}/\text{Cu})\text{O}_6$  octahedra are clearly distorted in BiT–0.08Cu and the tilt angle of Ti1–O3–Ti2 is  $156.8(6)^\circ$ . And the severely distorted  $\text{BiO}_{12}$  polyhedron consists of 12 Bi1–O bonds with seriously inequivalent bond lengths. The lengths of Bi–O bonds near the negative part of  $\text{Bi}^{3+}$  are longer than those near the positive part of  $\text{Bi}^{3+}$ . In the ferroelectric-phase structure, the defect dipoles would realign along the polarization axis when in equilibrium [53, 54]. In this case, the orientation of defect dipole  $(\text{V}_{\text{Bi}}'''-\text{V}_\text{O}^\bullet)'$  parallel to  $P_S$  is the most stable; i.e., the  $\text{V}_\text{O}^\bullet$  should be generated at the O3 site in the  $(\text{V}_{\text{Bi}}''' \text{O}_{11})$  polyhedron (middle, Fig. 9a). With  $\text{Cu}^{2+}$  acceptor substitution for the B-site  $\text{Ti}^{4+}$ , the resulting  $\text{V}_\text{O}^\bullet$  locates at the position 1 or 2 with an identical probability. Therefore, the orientation of  $(\text{Cu}_{\text{Ti}}''-\text{V}_\text{O}^\bullet)^{\text{X}}$  is questionable in the stable state because it cannot become collinear to  $P_S$  (right, Fig. 9a). The overall vector direction for different orientated defect dipoles of  $(\text{Cu}_{\text{Ti}}''-\text{V}_\text{O}^\bullet)^{\text{X}}$  in a small region (e.g., a ferroelectric domain) may be parallel to the overall  $P_S$ , i.e., induced defect polarization ( $P_D$ ) is parallel to the overall  $P_S$ . As a result, the migration of  $\text{V}_\text{O}^\bullet$  from one site to another can be considered as the reorientation of  $P_D$  in the lattice cell. In particular, the situation of  $P_S//P_D$  is with the lowest energy (left), and then value of  $P_S \perp P_D$  (middle) and  $P_S$  antiparallel to  $P_D$  (right) increases in order (Fig. 9b) [55]. Therefore, the long-range diffusion of  $\text{V}_\text{O}^\bullet$  becomes difficult, and BiT–100xCu shows a dramatic degradation in conductivity with higher  $E_a$  in the low-temperature segment.

EPR spectra as shown in Fig. 9c reveal the defect dipoles of  $(\text{Cu}_{\text{Ti}}''-\text{V}_\text{O}^\bullet)^{\text{X}}$  and  $(\text{Fe}_{\text{Ti}}'-\text{V}_\text{O}^\bullet)'$  in BiT–100xCu [51, 56]. It is well known that  $\text{Fe}^{3+}$  is one of the most abundant impurities in nature and can be detected in many oxides with EPR measurements. It is inferred that the source of hole conduction in BiT–0Cu is associated with the oxidation of  $\text{Fe}^{3+}$  to  $\text{Fe}^{4+}$  ( $\text{Fe}_{\text{Ti}}' + h \rightarrow \text{Fe}_{\text{Ti}}^{\text{X}}$ ). In our previous work [11], 1 at.% Nb substitution at the Ti site is sufficient to fill the oxygen vacancies at the perovskite lattices, and

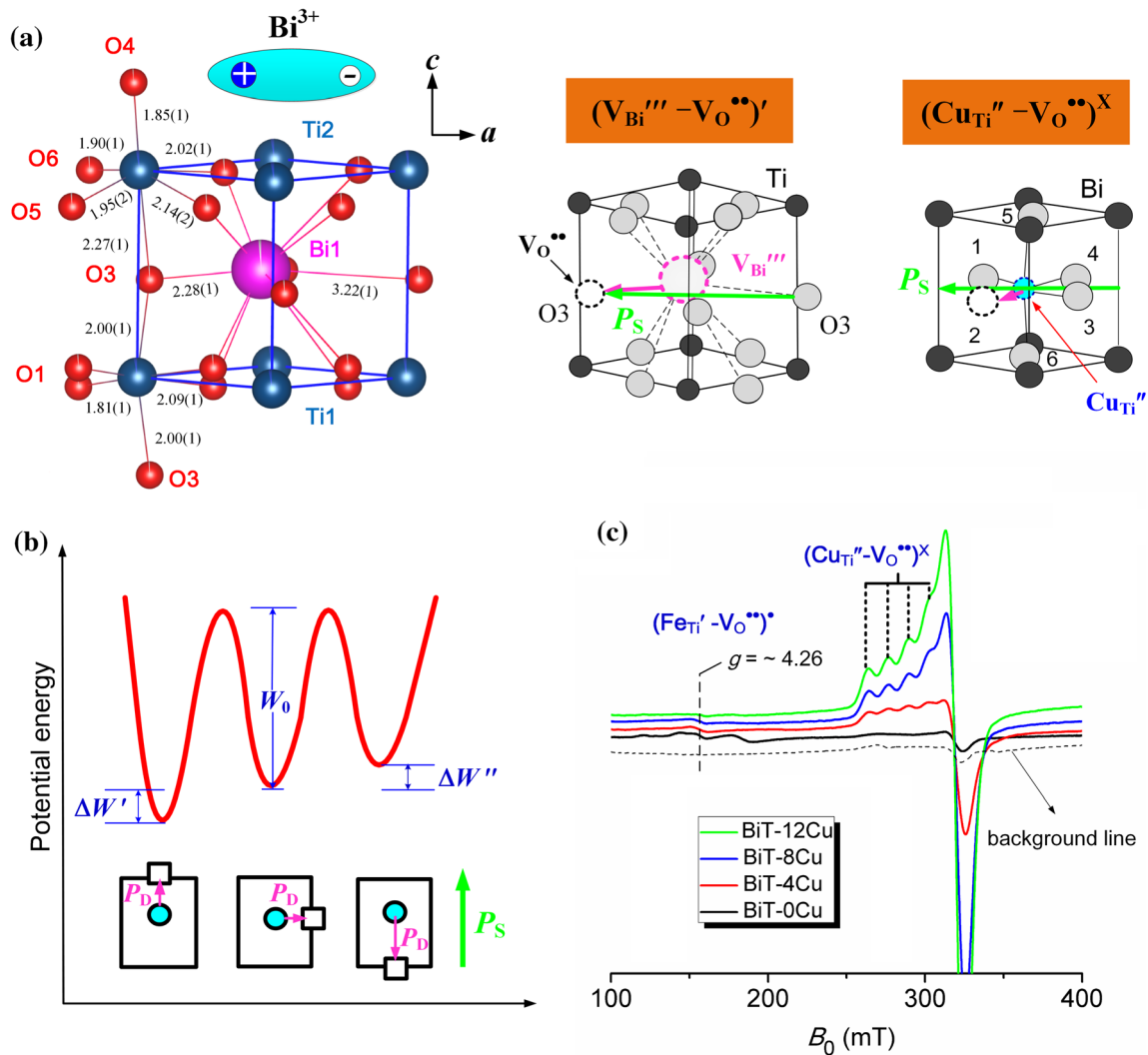


**Figure 9** **a** (Ti, Cu) $O_6$  octahedra and  $BiO_{12}$  polyhedron of BiT-8Cu and schematic illustrations of defect dipoles  $(V_{Bi}'''-V_O'')'$  and  $(Cu_{Ti}''-V_O'')^X$  orienting along the polarization axis ( $a$ -axis) in the orthorhombic symmetry. **b** Schematic formation energies of

consequently this Nb-substituted  $Bi_4Ti_3O_{12}$  shows significantly decreased  $\sigma_b$  and increased  $E_a$ . Here, the peak associated with  $(Fe_{Ti}'-V_O'')$  is not visible in the EPR spectrum of the Nb donor composition (inset of Fig. 9c). These results imply that the  $[V_O^\bullet]$  at the perovskite lattices in BiT-0Cu is about 0.15 at.%. For Cu-substituted compositions, the defect dipole  $(Cu_{Ti}''-V_O'')^X$  relative to  $(Fe_{Ti}'-V_O'')$  shows much higher peak intensity, indicating that  $Cu^{2+}$  concentration as well as its induced  $V_O^\bullet$  concentration is much higher than that of  $Fe^{3+}$  in the perovskite layers. Therefore, BiT-8Cu shows predominant ion conductivity in the bulk.

possibly orientated  $(Cu_{Ti}''-V_O'')^X$  in the  $(Cu_{Ti}''O_5\Box)$  octahedron. **c** EPR spectra of BiT-100xCu and  $Bi_4Ti_{2.97}Nb_{0.03}O_{12.015}$  (BiT-3Nb) with Nb donor substitution (inset) at 100 K.

## Conclusions

Polycrystalline ceramics of Cu-substituted  $Bi_4Ti_3O_{12}$  were prepared by a traditional solid-state reaction process. Structure, dielectric property and electrical conduction behaviors of the prepared  $Bi_4Ti_{3-x}Cu_xO_{12-x}$  (BiT-100xCu,  $x = 0, 0.04, 0.08,$  and  $0.12$ ) ceramics were investigated in detail. Crystal structure of representative BiT-8Cu was Rietveld refined based on neutron powder diffraction data. The structural refinement reveals that BiT-8Cu changes into an oxygen-deficient composition with a formula of  $Bi_{3.932}Ti_{2.929}Cu_{0.071}O_{11.832}$ . Impedance measurements under different oxygen atmospheres reveal that BiT-

OCu without Cu substitution ceramic shows oxygen-and-hole mixed conduction, whose  $\sigma_b$  is partially dependent on  $pO_2$ . With Cu acceptor substitution, modified BiT–100xCu ceramics have high oxide ion conductivity in the bulk due to the considerably increased  $V_O$  in the perovskite layers. The optimum composition of BiT–8Cu shows bulk ionic conductivity of  $\sim 0.007$  S/cm at 650 °C. This paper opens up new horizons for  $Bi_4Ti_3O_{12}$  as SOFCs materials operating at the intermediate temperature range.

## Acknowledgements

This work was supported by the National Natural Science Foundation of China (51502346, 51332003, 51903197), the Postdoctoral Science Foundation of China (2017M623165 and 2019T120904). We thank Dr. Yuanhua Xia (CAEP, Mianyang, China) for performing the neutron diffraction measurement.

## Compliance with ethical standards

**Conflict of interest** No conflict of interest exists in the submission of this manuscript. All the authors listed have approved the manuscript that is submitted. We declare that the work described is original research that has not been published previously, and not under consideration for publication elsewhere, in whole or in part.

## References

- [1] Damjanovic D (1998) Dielectric and piezoelectric properties of ferroelectric thin films and ceramics. *Rep Prog Phys* 61:1267
- [2] Park BH, Kang BS, Bu SD, Noh TW, Lee J, Jo W (1999) Lanthanum-substituted bismuth titanate for use in non-volatile memories. *Nature* 40(1):682–684
- [3] Lee HN, Hesse D, Zakharov N, Gosele U (2002) Ferroelectric  $Bi_{3.25}La_{0.75}Ti_3O_{12}$  Films of uniform a-axis orientation on silicon substrates. *Science* 296:2006–2009
- [4] Irie H, Saito H, Ohkoshi S, Hashimoto K (2005) Enhanced ferroelectric properties of nitrogen-doped  $Bi_4Ti_3O_{12}$  thin films. *Adv Mater* 17:491–494
- [5] Yang BB, Guo MY, Jin LH, Tang XW, Wei RH, Hu L, Yang J, Song WH, Dai JM, Lou XJ, Zhu XB, Sun YP (2018) Ultrahigh energy storage in lead-free  $BiFeO_3/Bi_{3.25}La_{0.75}Ti_3O_{12}$  thin film capacitors by solution processing. *Appl Phys Lett* 112:033904
- [6] Yan HX, Zhang HT, Reece MJ, Dong XL (2005) Thermal depoling of high curie point aurivillius phase ferroelectric ceramics. *Appl Phys Lett* 87:0829111
- [7] Cummins SE, Cross LE (1968) Electric and optical properties of ferroelectric  $Bi_4Ti_3O_{12}$  single crystals. *J Appl Phys* 39:2268–2274
- [8] Shulman HS, Damjanovic D, Setter N (2000) Niobium doping and dielectric anomalies in bismuth titanate. *J Am Ceram Soc* 83:528–532
- [9] Park BH, Hyun SJ, Bu SD, Noh TW, Lee J, Kim HD, Kim TH, Jo W (1999) Differences in nature of defects between  $SrBi_2Ta_2O_9$  and  $Bi_4Ti_3O_{12}$ . *Appl Phys Lett* 74:1907–1909
- [10] Long CB, Fan HQ, Li MM, Dong GZ, Li Q (2014) Crystal structure and enhanced electro-mechanical properties of aurivillius ferroelectric ceramics,  $Bi_4Ti_{3-x}(Mg_{1/3}Nb_{2/3})_xO_{12}$ . *Scr Mater* 75:70–73
- [11] Long CB, Chang Q, Fan HQ (2017) Differences in nature of electrical conduction among  $Bi_4Ti_3O_{12}$ -based ferroelectric polycrystalline ceramics. *Sci Rep* 7:4193
- [12] Tang YX, Shen ZY, Du QX, Zhao XY, Wang FF, Qin XM, Wang T, Shi WZ, Sun DZ, Zhou ZY, Zhang SJ (2018) Enhanced pyroelectric and piezoelectric responses in W/Mn-codoped  $Bi_4Ti_3O_{12}$  Aurivillius ceramics. *J Eur Ceram Soc* 38:5348–5353
- [13] Li XD, Chen ZN, Sheng LS, Li LL, Bai WF, Wen F, Zheng P, Wu W, Zheng L, Zhang Y (2019) Remarkable piezoelectric activity and high electrical resistivity in Cu/Nb co-doped  $Bi_4Ti_3O_{12}$  high temperature piezoelectric ceramics. *J Eur Ceram Soc* 39:2050–2057
- [14] Li XD, Chen ZN, Sheng LS, Du J, Bai WF, Li LL, Wen F, Zheng P, Wu W, Zheng L, Zhang Y (2019) Large enhancement of piezoelectric properties and resistivity in Cu/Ta co-doped  $Bi_4Ti_3O_{12}$  high-temperature piezoceramics. *J Am Ceram Soc* 102:7366–7375
- [15] Mahato N, Banerjee A, Gupta A, Omar S, Balani K (2015) Progress in material selection for solid oxide fuel cell technology: a review. *Prog Mater Sci* 72:141–337
- [16] Sengodan S, Choi S, Jun A, Shin H, Ju Y, Jeong H, Shin J, Irvine JTS, Kim G (2015) Layered oxygen-deficient double perovskite as an efficient and stable anode for direct hydrocarbon solid oxide fuel cells. *Nat Mater* 14:205–209
- [17] Duan C, Tong J, Shang M, Nikodemski S, Sers M, Ricotel S, Almansoori A, O'Hayre R (2015) Readily processed protonic ceramic fuel cells with high performance at low temperatures. *Science* 349:1321–1326
- [18] Malavasi L, Fisher CAJ, Islam MS (2010) Oxide-ion and proton conducting electrolyte materials for clean energy applications: structural and mechanistic features. *Chem Soc Rev* 39:4370–4387

- [19] Punn R, Feteira AM, Sinclair DC, Greaves C (2006) Enhanced oxide ion conductivity in stabilized  $\delta$ -Bi<sub>2</sub>O<sub>3</sub>. *J Am Chem Soc* 128:15386–15387
- [20] Sammes NM, Tompsett GA, Nafe H, Aldinger F (1999) Bismuth based oxide electrolytes-structure ionic conductivity. *J Eur Ceram Soc* 19:1801–1826
- [21] Garcia-Gonzalez E, Arribas M, Gonzalez-Calbet JM (2001) Short-range-long-range order transformation in the Bi<sub>4</sub>V<sub>2-x</sub>Fe<sub>x</sub>O<sub>11-y</sub> series. *Chem Mater* 13:96–102
- [22] Abrahams I, Krok F (2002) Defect chemistry of the bimevoxes. *J Mater Chem* 12:3351–3362
- [23] Abrahams I, Krok F, Malysb M, Wrobel W (2005) A model for the mechanism of low temperature ionic conduction in divalent-substituted  $\gamma$ -BIMEVOXes. *Solid State Ionics* 176:2053–2058
- [24] Singh P, Goodenough JB (2013) Monoclinic Sr<sub>1-x</sub>Na<sub>x</sub>SiO<sub>3-0.5x</sub>: new superior oxide ion electrolytes. *J Am Chem Soc* 135:10149–10154
- [25] Singh P, Goodenough JB (2012) Sr<sub>1-x</sub>K<sub>x</sub>Si<sub>1-y</sub>Ge<sub>y</sub>O<sub>3-0.5x</sub>: a new family of superior oxide-ion conductors. *Energy Environ Sci* 5:9626–9631
- [26] Atkinson A, Barnett S, Gorte RJ, Irvine JTS, McEvoy AJ, Mogensen M, Singhal SC, Vohs J (2004) Advanced anodes for high-temperature fuel cell. *Nat Mater* 3:17–27
- [27] Li M, Pietrowski MJ, De Souza RA, Zhang H, Reaney IM, Cook SN, Kilner JA, Sinclair DC (2014) A family of oxide ion conductors based on the ferroelectric perovskite Na<sub>0.5</sub>Bi<sub>0.5</sub>TiO<sub>3</sub>. *Nat Mater* 13:31–35
- [28] Yang F, Zhang HR, Li LH, Reaney IM, Sinclair DC (2016) High ionic conductivity with low degradation in A-site strontium doped nonstoichiometric sodium bismuth titanate perovskite. *Chem Mater* 28:5269–5273
- [29] Bhattacharyya R, Das S, Omar S (2018) High ionic conductivity of Mg<sup>2+</sup>-doped non-stoichiometric sodium bismuth titanate. *Acta Mater* 159:8–15
- [30] Takahashi M, Nguchi Y, Miyayama M (2002) Electrical conduction mechanism in Bi<sub>4</sub>Ti<sub>3</sub>O<sub>12</sub> single crystal. *Jpn J Appl Phys* 41:7053–7056
- [31] Takahashi M, Nguchi Y, Miyayama M (2004) Estimation of ionic and hole conductivity in bismuth titanate polycrystals at high temperatures. *Solid State Ionics* 172:325–329
- [32] Xie X, Wang T, Zhou Z, Cheng G, Liang R, Dong X (2019) Enhanced piezoelectric properties and temperature stability of Bi<sub>4</sub>Ti<sub>3</sub>O<sub>12</sub>-based Aurivillius ceramics via W/Nb substitution. *J Eur Ceram Soc* 39:957–962
- [33] Hou JG, Kumar RV, Qu YF, Krsmanovic D (2009) B-site doping effect on electrical properties of Bi<sub>4</sub>Ti<sub>3-2x</sub>Nb<sub>x</sub>Ta<sub>x</sub>O<sub>12</sub> ceramics. *Scr Mater* 61:664
- [34] Wang T, Liao Y, Wang D, Zheng Q, Liao J, Xie F, Jie W, Lin D (2019) Cycling- and heating-induced evolution of piezoelectric and ferroelectric properties of CuO-doped K<sub>0.5</sub>Na<sub>0.5</sub>NbO<sub>3</sub> ceramic. *J Am Ceram Soc* 102:351–361
- [35] Lotgering FK (1959) Topotactical reactions with ferrimagnetic oxides having hexagonal crystal structures-I. *J Inorg Nucl Chem* 9:113–123
- [36] Shannon RD (1976) Revised effective ionic radii and systematic studies of interatomic distances in halides and chalcogenides. *Acta Crystallogr A* 32:751–767
- [37] Hashimoto T, Moriwake H (2008) Oxygen vacancy formation energy and its effect on spontaneous polarization in Bi<sub>4</sub>Ti<sub>3</sub>O<sub>12</sub>: a first-principles theoretical study. *Phys Rev* 78:092106
- [38] Withers RL, Thompson JG, Rae AD (1991) The crystal chemistry underlying ferroelectricity in Bi<sub>4</sub>Ti<sub>3</sub>O<sub>12</sub>, Bi<sub>3</sub>TiNbO<sub>9</sub>, and Bi<sub>2</sub>WO<sub>6</sub>. *J Solid State Chem* 94:404–417
- [39] Sivakumar T, Itoh M (2011) Ferroelectric phase transitions in new Aurivillius oxides: Bi<sub>2+2x</sub>Sr<sub>1-2x</sub>Nb<sub>2-x</sub>Sc<sub>x</sub>O<sub>9</sub>. *J Mater Chem* 21:10865–10870
- [40] Shimakawa Y, Kubo Y, Nakagawa Y, Goto S, Kamiyama T, Asano H, Izumi F (2000) Crystal structure and ferroelectric properties of ABi<sub>2</sub>Ta<sub>2</sub>O<sub>9</sub> (Ca, Sr, and Ba). *Phys Rev B* 61:6559–6564
- [41] Fouskova A, Cross LE (1970) Dielectric properties of bismuth titanate. *J Appl Phys* 41(7):2834–2838
- [42] Islam MS (2002) Computer modelling of defects and transport in perovskite oxides. *Solid State Ionics* 154–155:75–85
- [43] Irvine JTS, Sinclair DC, West AR (1990) Electroceramics: Characterization by impedance spectroscopy. *Adv Mater* 2:132–138
- [44] Masó N, West AR (2012) Electrical properties of Ca-doped BiFeO<sub>3</sub> ceramics: from *p*-type semiconduction to oxide-ion conduction. *Chem Mater* 24:2127–2132
- [45] Takahashi M, Nguchi Y, Miyayama M (2003) Effects of V-doping on mixed conduction properties of bismuth titanate single crystals. *Jpn J Appl Phys* 42:6222–6225
- [46] Li M, Zhang HR, Cook SN, Li LH, Kilner JA, Reaney IM, Sinclair DC (2015) Dramatic influence of A-site nonstoichiometry on the electrical conductivity and conduction mechanisms in the perovskite oxide Na<sub>0.5</sub>Bi<sub>0.5</sub>TiO<sub>3</sub>. *Chem Mater* 27:629–634
- [47] Jamnik J, Maier J (1999) Treatment of the impedance of mixed conductors equivalent circuit model and explicit approximate solutions. *J Electrochem Soc* 146(11):4183–4188
- [48] Yoon SH, Randall CA, Hur KH (2009) Effect of acceptor (Mg) concentration on the resistance degradation behavior in acceptor (Mg)-doped BaTiO<sub>3</sub> bulk ceramics: I. Impedance analysis. *J Am Ceram Soc* 92(8):1758–1765

- [49] Lee S, Randall CA (2013) Determination of electronic and ionic conductivity in mixed ionic conductors: HiTEC and in situ impedance spectroscopy analysis of isovalent and aliovalent doped BaTiO<sub>3</sub>. *Solid State Ionics* 249–250:86–92
- [50] Kim N, Grey CP (2002) Probing oxygen motion in disordered anionic conductors with 17O and 51 V MAS NMR spectroscopy. *Science* 297:1317–1320
- [51] Islam MS (2000) Ionic transport in ABO<sub>3</sub> perovskite oxides: a computer modelling tour. *J Mater Chem* 10:1027–1038
- [52] Kim N, Vannier RN, Grey CP (2005) Detecting different oxygen-ion jump pathways in Bi<sub>2</sub>WO<sub>6</sub> with 1- and 2-dimensional 17O MAS NMR spectroscopy. *Chem Mater* 17:1952–1958
- [53] Ren XB (2004) Large electric-field-induced strain in ferroelectric crystals by point-defect-mediated reversible domain switching. *Nat Mater* 3:91–94
- [54] Ke SM, Huang HT, Fan HQ, Lee HK, Zhou LM (2012) Antiferroelectric-like properties and enhanced polarization of Cu-doped K<sub>0.5</sub>Na<sub>0.5</sub>NbO<sub>3</sub> piezoelectric ceramics. *Appl Phys Lett* 101:082901
- [55] Eichel RA (2011) Structural and dynamic properties of oxygen vacancies in perovskite oxides-analysis of defect chemistry by modern multi-frequency and pulsed EPR techniques. *Phys Chem Chem Phys* 13:368–384
- [56] Eichel RA (2007) Defect structure of oxide ferroelectrics-valence state, site of incorporation, mechanisms of charge compensation and internal bias fields. *J Electroceram* 19:9–21

**Publisher's Note** Springer Nature remains neutral with regard to jurisdictional claims in published maps and institutional affiliations.